Proposal of a new low-cycle fatigue life model for cast iron with room temperature calibration involving mean stress and high-temperature effects

Research paper

Corresponding Author:
Raffaella Sesana, Politecnico di Torino, Corso duca degli Abruzzi 24, 10129 Torino, Italy
Email: raffaella.sesana@polito.it

Proposal of a new LCF life model for cast iron with room temperature calibration involving mean stress and high temperature effects

Cristiana Delprete, Raffaella Sesana*

Politecnico di Torino, Department of Mechanical and Aerospace Engineering

Corso duca degli Abruzzi 24, 10129 Torino, Italy

Abstract

The paper presents and discusses a low cycle fatigue (LCF) life prediction energy-based model. The model was applied to a commercial cast iron automotive exhaust manifold. The total expended energy until fracture proposed by the Skelton model was modified by means of two coefficients which take into account of the effects of mean stress and/or mean strain, and the presence of high temperature. The model was calibrated by means of experimental tests developed on Fe-2.4C-4.6Si-0.7Mo-1.2Cr high temperature-resistant ductile cast iron. The thermo-structural transient analysis was developed on a finite elements (FE) model built to overtake confidentiality industrial restrictions. In addition to the commercial exhaust manifold, the FE model considers the bolts, the gasket and a cylinder head simulacrum to consider the corresponding thermal and mechanical boundary conditions. The life assessment performance of the energy-based model with respect the cast iron specimens was compared with the corresponding Basquin-Manson-Coffin and Skelton models. The model prediction fits the experimental data with a good agreement, which is comparable with both the literature models and it shows a better fitting at high temperature. The life estimations computed with respect the exhaust manifold FE model were compared with different multi-axial literature life models and literature data to evaluate the life prediction capability of the proposed energy-based model.

* corresponding author, raffaella.sesana@polito.it

Keywords

LCF, Cast iron, Damage, Life estimation, Exhaust manifold

Nomenclature

K_s	Total material energy expenditure until fracture (sum of the areas of all hysteresis loops until failure [J/m^3] [MPa])
N_f	Number of cycles to failure
N_{exp}	Average experimental number of cycles to failure
N	Estimated number of cycles to failure
$diff\%$	% difference of number of cycles to failure between experimental and estimated
σ	Stress [MPa]
σ_m	Mean stress in cyclic loading [MPa]
σ_a	Alternate stress in cyclic loading [MPa]
$\sigma_{a,eq-1}$	Equivalent stress amplitude corresponding to fully-reversed loading [MPa]
σ_{max}	Maximum tensile stress achieved in the application or in cyclic loading [MPa]
σ_{min}	Maximum tensile stress achieved in the application or in cyclic loading [MPa]
σ'_f	Fatigue strength coefficient (Basquin-Manson-Coffin equation)
ε	Strain [-]
ε_m	Mean strain in cyclic loading [-]
ε_a	Alternate strain in cyclic loading [-]
$\varepsilon_{a,eq-1}$	Equivalent strain amplitude corresponding to the fully-reversed loading [-]
ε'_f	Fatigue ductility coefficient (Basquin-Manson-Coffin equation)
$\varepsilon_{a,tot}$	Total strain amplitude [-]
η, ξ	Coefficient for material sensitivity to mean stress-strain
h, k	Material parameters
U_i	Specific energy dissipated per cycle (half-life) in experimental conditions [J/m^3] [MPa]
f_{ms}	Correction coefficient related to the mean stress or strain [-]
f_{ht}	Correction coefficient related to the high temperature isothermal effects [-]
n	Material parameter [-]
UTS	Ultimate tensile strength of the material [MPa]
T	Temperature [°C]

T_{act}	Activation temperature for creep [°C]
T_m	Mean temperature achieved in the application [°C]
$T_{\max}$	Maximum temperature achieved in the application [°C]
T_{mlt}	Material melting temperature [°C]
A	Amplitude ratios σ_a/σ_m and $\varepsilon_a/\varepsilon_m$
R	Stress ratio $\sigma_{\min}/\sigma_{\max}$
b	Fatigue strength exponent (Basquin-Manson-Coffin equation)
c	Fatigue ductility exponent (Basquin-Manson-Coffin equation)
E	Material longitudinal elastic modulus [MPa]

1. Introduction

The current consolidated trend to reduce fuel consumption and emissions and to increase performances, with the aim to meet the international Standards and the market demands, has introduced new problems in the fatigue design process of engine components.

The ever-increasing temperature reached by engine components plays a fundamental role on the evolution of the mechanical properties of materials and the fatigue life expected under such working conditions is usually shorter than 10^4 cycles, proper of the LCF regime. Furthermore, if the temperature varies in time simultaneously with the mechanical load, Thermo-Mechanical Fatigue (TMF) condition is present and the interactions between thermal and mechanical fields become complex. After the component stress-strain field was computed by numerical simulation or measured during experimental activities, the final demand is to predict its working life. This operation is nowadays still tricky and not completely clear because the interaction between mechanical fatigue, creep and oxidation may results in a very different influence on fatigue life, depending mainly on material and loading history. The scientific literature provides a wide variety of damage models characterized by different degrees of complexity and life prediction capabilities; some of them are of general validity, other purposely developed to be applied in very specialized applications. In general, a damage model has to satisfy three fundamental requirements, particularly important especially from an industrial point of view as simple formulation, which allows an easy implementation; small number of parameters to be estimated, with obvious advantages in terms of experimental effort and good prediction capabilities.

Without assuming to be exhaustive, a deep and complete review on high temperature LCF and TMF damage and life models, whose main categories are summarized in [1], can be found in [2, 3, 4] for

physical models, in [5, 6, 7, 8] for empirical models, in [9, 10, 11] for damage mechanics models, in [12, 13, 14, 15, 16, 17, 18, 19] for fracture mechanics models, and in [20, 21, 22, 23, 25, 26, 29] for energy-based models.

In particular [2, 3, 4] physical models consider all physical phenomena involved in fatigue damage, modelling through analytical relations. According to [17] he significance of physical models for TMF life prediction is rather low, as modelling the interaction of damage mechanisms, where still some fundamental physical concepts are not completely clear and understood, is still critical. However, the importance of the physical approach lies primarily in providing the physical background for empirical and damage mechanics models, e.g. by explaining the conditions which promote the formation of cavities.

Empirical models [5, 6, 7, 8], from an industrial point of view, consist in a practical alternative to sophisticated and expensive calibration procedures, of analytical models. Therefore, the empirical approach is often used and preferred in practical application for design purposes, achieving at any rate a good agreement between experimentally observed LCF and TMF life and the data predicted by means of empirical models.

Damage mechanics models [9, 10, 11] are usually based on the definition of a mechanical damage variable representative of the state of deterioration of the material [11]. The difficulty of this task lies in the fact that macroscopically there is nothing that distinguishes a highly damaged volume element from a virgin one; it follows that several internal variables corresponding to the damaged state of the material have to be introduced, which can be related to the microstructure, such as the density of microcracks and cavities, or to global measurements, such as mass density and resistivity, or to mechanical measurements, such as the modification of elastic, plastic or viscoplastic properties. The concept of damage mechanics is rarely applied to complex loading, such as TMF.

Fracture mechanics models [12, 13, 14, 15, 16, 17, 18, 19] describe the growth of a fatal crack from its initial size to its final size at failure. These methods are preferentially applicable if a material contains defects from the start or if cracks are initiated quickly at the beginning of cyclic life [17]. The local conditions at or in the vicinity of the crack tip are considered to be responsible for crack propagation. The advantage this approach consists in crack length which represents a physically measurable quantity of damage. Furthermore, the implications of microstructural changes can directly be considered in modelling.

Several damage models based on energetic approaches were also proposed as for example [20-29]. The basic observation is that, on the microscopic level, the cyclic plastic strain is related to the movement of dislocations, and the cyclic stress is related to the resistance to their motion. Thus, the plastic strain energy per cycle can be regarded as a measure of the amount of LCF damage per

cycle, while the fatigue resistance of the material may be characterized in terms of its capacity to absorb and dissipate plastic strain energy. An energy-based life model can potentially achieve high prediction capabilities since the hysteresis loop takes into account of the effects of damage related phenomena and their interactions. Nevertheless, two issues must be considered, temperature and mean value of stress (strain) influence on LCF life are not explicitly considered.

In [30] a mean stress sensitivity factor is defined for HCF application for many materials and also for cast iron. In case of LCF the model neglects the mean stress effect as the large amount of plastic strain tends to reduce the mean stress effect. In [31] the mean plastic strain effect is considered and taken into account by means of strain energy density parameters. This model showed good prediction in case of cast iron undergoing high temperatures. In [32] the equilibrium conditions for loading and unloading phases in HCF are calculated as a function of the dislocation density, resulting in an expression for the plastic strain increment at each loading step. Since the model directly include the shear modulus and the specific fracture energy for unit area (both temperature dependent quantities), it is able to indirectly include the effects of temperature. However, despite some development of this model for multi-scale simulations [33, 35] and its mathematical affinity with previous empirical models [36], its application to LCF has been blocked by the lack of cyclic hardening phenomena which is among the model assumptions.

In the last years, among empirical models, the energetic approaches have found diffusion in literature. The strain energy density approach assumes that the fatigue failure occurs when the total strain energy density (TSED) at the initiation sites reaches a critical value. In case of notched specimens, they experience the same lives if the stress-strain histories at the initiation sites are the same. In [37] the research applies the TSED approach for estimating life of notched samples under multiaxial fatigue loading. To reduce experimental costs, the procedure is based on a master curve obtained from uniaxial fatigue tests on standard smooth specimens using smooth standard specimens, as TSED versus number of cycles to failure. The master curve is calibrated by means of HCF and LCF cyclic tests with stress ratio R=−1. The influence of temperature and mean stress is not considered. The correlation between experimental and estimated cycles to failure is good.

Several papers are dedicated to life model based on crack propagation. For example, in [38] a volume-based strain energy density (VSED) approach applied to static and fatigue strength assessment of notched and welded structures. In this approach, an elementary volume is defined stating that the effective parameter to define the strength and the crack propagation is the notch stress averaged over a short distance normal to the notch edge and not the theoretical maximum notch stress. The approach allows to quantify the strain energy density in case of multiaxial stress and strain situations, as in notches and welded joints, basing on geometrical and material

parameters. The VSED approach well adapt to multiaxial stress conditions. In the mentioned paper, the model calibration has no references with respect to high temperature.
In [38] a strain energy density (SED) approach is applied to creep-fatigue problems. The SED necessary to cause failure in standard rupture tests including tertiary creep is a function of stress value and of the elongation at failure. In this approach the threshold values require to be found at each temperature and stress condition by means of dedicated calibration tests. In [39] the same SED approach applied to creep problem is extended to oxidation damage due to high temperature by means of corrective factors in case of compressive and tensile creep loading.
In addition, several purely multi-axial damage/life criteria are proposed with the aim to estimate fatigue life in LCF regime for mechanical components, when the stress state is complex. An overview of the main multi-axial models can be found in [40-46]. However, according to [47], the Basquin-Manson-Coffin (BMC) model results to be the most suitable for isothermal LCF applications of cast iron.
The general lack of literature models is the description of sensitivity of models to parameter calibration with temperature. Generally speaking, literature models are calibrated in testing or working conditions but very few are described related to estimation in temperature testing and working conditions different from calibration ones.
The present paper proposes an energy-based life model containing two factors purposely introduced to consider high temperature and mean stress or strain effects, with the aim to improve the life prediction capability. The analytical background is presented together with the calibration procedure to determine the values of the model parameters. The model is applied to a specific case-study of a commercial exhaust manifold made by the high temperature-resistant Si-Mo-Cr ductile cast iron Fe-2.4C-4.6Si-0.7Mo-1.2Cr, whose experimental characterization is reported in [45].
The estimation of the residual life is computed applying an *ad-hoc* Matlab ® numerical code [46] and the life prediction achieved is finally compared with those obtained using literature multi-axial damage models. The main goal during the overall research activity was the development of a life model suitable for a fast and direct use for industrial applications. It resulted that the aims to be achieved were: introduction of a small number of parameters, calibration by means of as simple as possible experimental tests, agreement with physical observations, and high prediction capability.

2. Analytical background

The here proposed CIEL (Cast Iron Life Energy-based) model refers to the well-known experimental observation regarding the cumulative (or total) energy expenditure until fracture. As documented by Skelton [26, 29], this amount of total expended energy is a material constant almost

independent by the strain range applied and dependent only by the temperature.
The hysteresis loop area represents a measure of this energy expenditure and consequently, limited to testing isothermal conditions, a material related constant value K_s can be calculated as the sum of the areas of all the hysteresis loops until failure,

$$K_s = \sum_{i=1}^{Nf} \oint_i \sigma \, d\varepsilon \tag{1}$$

where i is the generic hysteresis cycle.
When the value of K_s is known, the number of cycles to failure can be predicted as,

$$N_f = \frac{K_s}{U_i} \tag{2}$$

where U_i is the specific energy dissipated per cycle in experimental conditions according to application under investigation.
According to [26], during LCF tests at constant total strain range and high temperature, the cumulative hysteresis energy absorbed to failure K_s is constant and effectively independent of strain range. In addition, for a given total strain range, the hysteresis energy per cycle U_i is almost independent of the stage of hardening or softening.
The K_s parameter can potentially take into account of all the damaging factors influencing the fatigue life, because these latter contribute for defining shape and size of hysteresis loops. However, the effect of mean stress and/or mean strain is not explicitly considered. Furthermore, the second drawback is related to the only partial consideration of the high temperature effects on fatigue, such as creep and oxidation, during the computation of the cycles area, which may lead the model to be overpredicting.
To improve the prediction capabilities of the model, to correct the value of the total expended energy until fracture K_s computed in symmetrical LCF tests with no mean stress and at a fixed temperature level conditions, two coefficients are introduced: f_{ms} related to the mean stress or strain (stress-strain in the following), and f_{ht} related to the high temperature isothermal effects. It is then possible to determine the value of K_s by a single test and to correct it to suit several conditions.
The proposed formulation of CIEL model is then,

$$N_f = \frac{K_S}{U_i} f_{ms} \cdot f_{ht} \tag{3}$$

and its advantages are mainly three:

- The energy-based model proposed by Skelton [26] can be used also in presence of mean stress and high temperature applications different from calibration condition;
- The expended energy to failure can be measured under a single test condition, i.e. imposing a single strain range at room temperature;
- To calibrate the model only five parameters are introduced and the calibration procedure is direct.

In the CIEL model, failure is intended as crack nucleation.

2.1. Mean stress-strain effect

The most general situation which can be detected during a fatigue calculation is represented by a stabilized hysteresis loop given a mean stress σ_m and/or mean strain ε_m different from zero. It is widely accepted that, for metals, a tensile mean stress-strain is usually detrimental while a compressive one is beneficial for the fatigue life itself.

To determine a suitable stress/strain correction coefficient to use in fatigue calculation, the works of Fang [4039], Kujawski and Ellyin [48], Chu [47] and Dowling [49] provide important contributions. In particular [4039] presents a unified approach assuming that the damage caused by cyclic loading is a function of the strain energy, i.e. a function of both stress and strain.

Mean stress-strain effect can be introduced as a function of the ratio between the mean stress-strain to the alternate stress-strain,

$$f\left(\frac{\sigma_m}{\sigma_a}\right) = \left(1 + \eta \frac{\sigma_m}{\sigma_a}\right)^h \quad \text{and} \quad f\left(\frac{\varepsilon_m}{\varepsilon_a}\right) = \left(1 + \xi \frac{\sigma_m}{\sigma_a}\right)^k \tag{4}$$

where coefficients $\eta \geq 0$ and $\xi \geq 0$ characterize the material sensitivity to mean stress-strain, and $h \geq 0$ and $k \geq 0$ are material parameters.

Equations (4) lead to the following relations,

$$\sigma_{a,eq-1} = \sigma_a \left(1 + \eta \frac{\sigma_m}{\sigma_a}\right)^h \quad \text{and} \quad \varepsilon_{a,eq-1} = \varepsilon_a \left(1 + \xi \frac{\varepsilon_m}{\varepsilon_a}\right)^k \tag{5}$$

where subscript *-1* refers to the fully-reversed loading path corresponding to the stress ratio $R = -1$, and stress $\sigma_{a,eq-1}$ and strain $\varepsilon_{a,eq-1}$ can be interpreted as equivalent stress and strain amplitude corresponding to the fully-reversed loading.

The two contributions can further define a unique function, appropriate for LCF isothermal regime, which corresponds to the coefficient f_{ms} of Eq. (3),

$$f_{ms} = f\left(\frac{\sigma_m}{\sigma_a}, \frac{\varepsilon_m}{\varepsilon_a}\right) = \left[\left(1+\eta\frac{\sigma_m}{\sigma_a}\right)^h \cdot \left(1+\xi\frac{\varepsilon_m}{\varepsilon_a}\right)^k\right]^{-1} \quad (6)$$

where coefficients η, h, ξ, and k are calibrated through LCF isothermal tests.

It can be noted that,

- If $\sigma_m > 0$ and/or $\varepsilon_m > 0$ (tensile mean stress or strain) then $f_{ms} < 1$,

K_s decreases and fatigue life decreases with respect of fully-reversed loading paths;

- If $\sigma_m < 0$ and/or $\varepsilon_m < 0$ (compressive mean stress or strain) then

$f_{ms} > 1$, K_s increases and fatigue life increases with respect of fully-reversed loading paths;

- If $\sigma_m = 0$ and/or $\varepsilon_m = 0$ then $f_{ms} = 1$.

The numerical nonlinear relation between coefficient f_{ms} and mean stress-strain is reported as example in Figure 1.

This evolution of the coefficient f_{ms} is then coherent with the physics of the problem.

Moreover, analyzing Equation (6) it is possible to see that, keeping h and k, an increase of η and ξ results in an increase of the term f_{ms} for compressive mean stresses and a decrement of the coefficient for positive mean stresses. At the same manner, an increase of the exponents h and k results in an increase of f_{ms} for compressive mean stresses and a decrement of the coefficient for positive mean stresses.

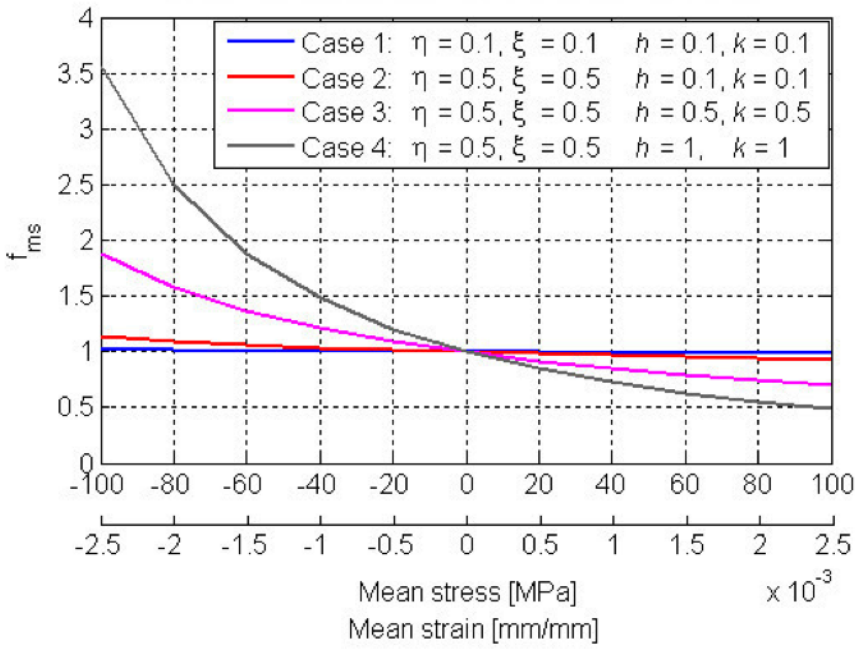

Figure 1, Nonlinear evolution of the mean stress-strain coefficient f_{ms}.

2.2. High temperature effect

In general, if a component is subjected to high temperature working conditions, both creep and oxidation phenomena may influence damage. The coefficient here proposed to correct the total expended energy until fracture K_s taking into account of high temperature effects, was developed focusing on creep only, neglecting oxidation effect. Oxidation, in fact, affects the superficial crack nucleation phase and the material properties of a thin external layer. On the contrary, creep damage affects the bulk material with progressive phenomena, influencing the material behaviour, the plastic accumulation, and the energy accumulation before crack nucleation. If a conservative approach and a value of energy before crack nucleation are required, the phenomena related to oxidation have to be considered separately as they involve an una-tantum phenomenon while creep damage is a progressive one.

To write a suitable coefficient taking into account of high temperature effect, the attention was focused on the most widely accepted theories used to model the secondary creep stage, such as [50-63].

The stress influence on secondary creep stage can be successfully modelled through the power laws proposed by Norton [52], and Harper and Dorn [57]. A dimensionless coefficient to be multiplied by the constant K_s is related to the ratio between the maximum stress influence on creep, which can be reached in the application under investigation, and the maximum stress influence, which can be experienced by the material. This means comparing the component operating condition with the material testing condition.

It results that in the Norton creep law the influence $f(\sigma)$ of stress on the secondary creep stage can be expressed as a power law,

$$f(\sigma) = \left(\frac{\sigma_{max}}{UTS}\right) \tag{7}$$

where σ_{max} is the maximum tensile stress achieved in the application analysed, *UTS* the ultimate tensile strength of the material, and *n* a material parameter.

On the other hand, the temperature influence *f(T)* on creep can be modelled using an Arrhenius-type relation. In analogy with the approach followed to define the mean stress-strain influence, also a specific ratio is introduced for the temperature effects,

$$f\left(T\right)=\frac{e^{-\frac{T_{act}-T_m}{T_{\max}}}}{e^{-\frac{T_{\max}}{T_{mlt}}}} \tag{8}$$

where T_{act} is the activation temperature for creep (about 1/3 of the melting temperature T_{mlt} of the material), T_m and T_{max} the mean and the maximum temperature achieved in the application considered.

This temperature coefficient correlates the variables related to the component under investigation (T_m and T_{max}) with the variable related to the material (T_{mlt}). The advantage of this formulation lies in taking into account of the activation temperature for creep phenomena.

According to the experimental evidence, under the threshold temperature of $T_{mlt}/3$ creep can be neglected while above this limit the creep related damage increases exponentially. It follows that the complete coefficient proposed to take into account of temperature effects on fatigue is,

$$f_{ht}=\left[1+\left[\left(\frac{\sigma_{\max}}{UTS}\right)^{n}\cdot\frac{e^{-\frac{T_{act}-T_m}{T_{\max}}}}{e^{-\frac{T_{\max}}{T_{mlt}}}}\right]\right] \tag{9}$$

which can be also lower than the unit value (< 1) if the maximum tensile stress is compressive. In this case creep phenomena are obstructed and the total expended energy until fracture K_s is increased, with an increment of the fatigue life according to the experimental observations.

Moreover, to model the actual trend of the coefficient which increases rapidly if the mean temperature of the component working condition is higher than the activation temperature, the exponent *b*, which can be calibrated through experimental data, was introduced.

Figure 2 shows the numerical simulation of the evolution of the high temperature coefficient f_{ht} in function of the mean temperature.

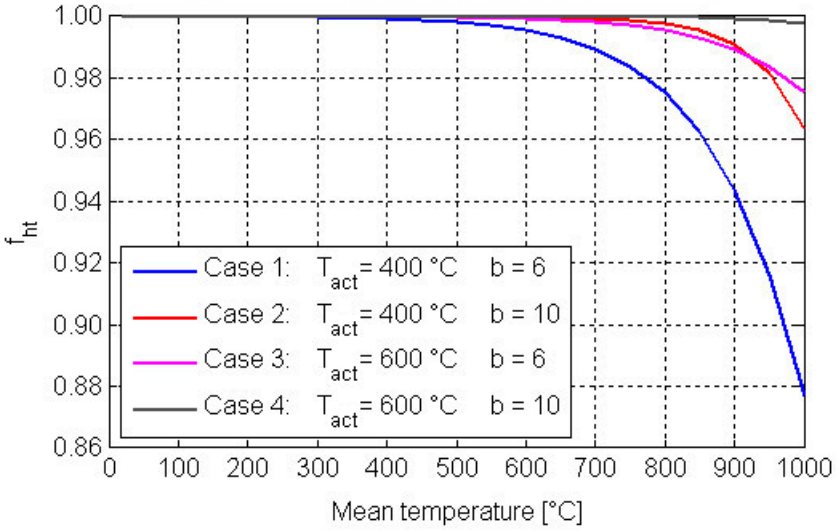

Figure 2, Nonlinear evolution of the high temperature coefficient f_{ht}.

The plot shows that for working mean temperature below the activation temperature, the coefficient f_{ht} is close to one, with a negligible influence on the constant K_s and consequently on the life of the component. On the other hand, if the working mean temperature is higher than the activation temperature, the coefficient f_{ht} rapidly decreases and the life of the component decreases, according to Equation (3).

3. Model calibration

The investigated material is a commercial SiMo cast iron used for automotive exhaust manifold manufacturing, which composition is reported in Table 1. Specimens were obtained from sprues coming from the casting process of automotive exhaust manifolds. Before specimens machining, the cast iron sprues underwent a thermal treatment in order to obtain an alloy microstructure as similar as possible to the material of actual exhaust manifolds. In Figure 3 the microstructure of the specimen material after thermal treatment is presented. The image obtained at the 100× magnification shows density, size and distributions of the graphite nodules. Graphite nodules are characterized by a mean radius of about 13 µm and 140 nodules/mm^2, the mean size of the grains is 50 µm. Pearlite formation occurred at the ferrite grain boundaries, as it is particularly evident in 500× magnification. The presence of pearlite increases the strength of the alloy but decreases the ductility, in particular at room temperature. The scratch on the right of the left image has a reference function.

Table 1: SiMo cast iron composition (weight percent)

C	Si	Mn	P	S	Cr	Mo	Ni	Mg	Cu
2.45	4.60	0.24	0.02	0.01	1.18	0.75	0.02	0.04	0.03

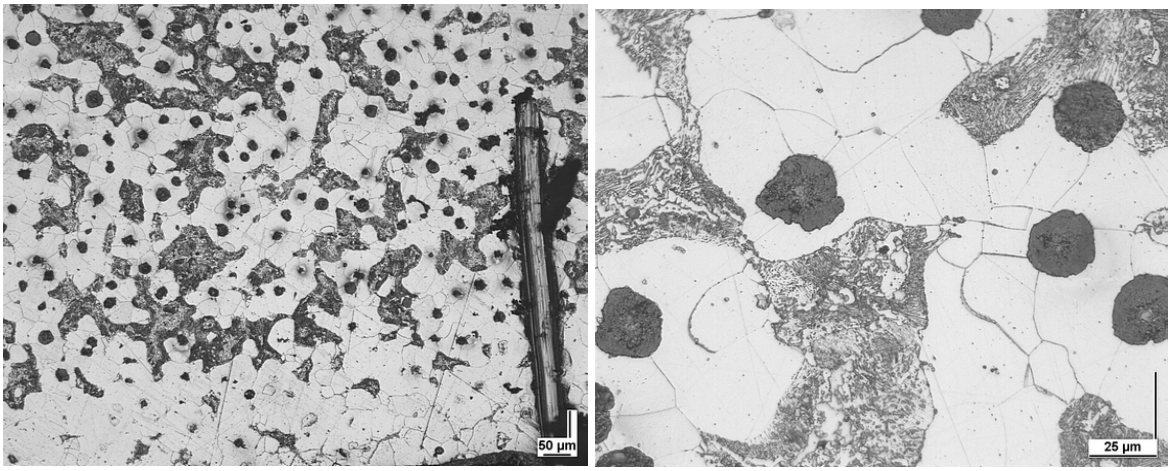

Figure 3: specimen material microstructure: 100X (left) and 500X (right) magnification

Static material characterization was obtained at room temperature, 160 °C, 500 °C, and 800 °C on circular dogbone specimens. Strain was measured by means of an extensometer. The Young Modulus has been estimated through a linear regression which interpolates the experimental data belonging to the elastic field. The yield stress was calculated as the intersection between the tensile curve and a line parallel to the elastic field regression starting from 0.2% of total strain, while for the *UTS* the maximum stress achieved during the test has been considered, according to the ASTM Standard E 8/E 8M [58]. Each data is the average of results obtained on at least five specimens. The complete testing campaign is described in detail in [45]. The results are summarized in Table 2. The thermal expansion coefficient was determined, and the results are presented in Table 3.

Table 2: static material properties at different temperatures

	Young Modulus E	**Yield stress** σ_y	**Ultimate tensile strenght** *UTS*
Room temperature	178.1 ± 2.4 GPa	549 MPa	608 MPa
160 °C	173.3 ± 2.3 GPa	533 MPa	594 MPa
500 °C	141.1 ± 2.7 GPa	245 MPa	352 MPa
800 °C	115.7 ± 2.2 GPa	153 MPa	154 MPa

Table 3: Thermal expansion coefficient values

Temperature range	**Thermal expansion coefficient [1/°C]**
20°C - 200°C	$1.28 \cdot 10^{-5}$
200°C - 400°C	$1.46 \cdot 10^{-5}$
400°C - 800°C	$1.61 \cdot 10^{-5}$

The overall calibration and model validation testing campaign was developed according to

standards and literature, for example [59], on circular dogbone specimens. The complete testing campaign is described in detail in [45]. In particular, HCF testing results are reported in Table 4. Specimen geometry is reported in Figure 4.

Table 4: HCF staircase results at 160 °C, 500 °C, 800 °C.

Fatigue limit	% failures	160 °C [MPa]	500 °C [MPa]	800 °C [MPa]
σ_{max}	50	185	116	74
standard deviation *s*		5	7	7
σ_{max}	90	178	107	65
σ_{max}	10	192	125	83
$\sigma_{D0.1}$	50	83	52	33
standard deviation *s*	50	2	3	3
$\sigma_{D0.1}$	90	80	48	29
$\sigma_{D0.1}$	10	86	56	37
σ_{D-1} according to Gerber's model				
σ_{D-1}	50	86	53	34
σ_{D-1}	90	82	49	30
σ_{D-1}	10	89	57	38
σ_{D-1} according to modified Goodman's model				
σ_{D-1}	50	123	78	55
σ_{D-1}	90	117	71	47
σ_{D-1}	10	128	85	65

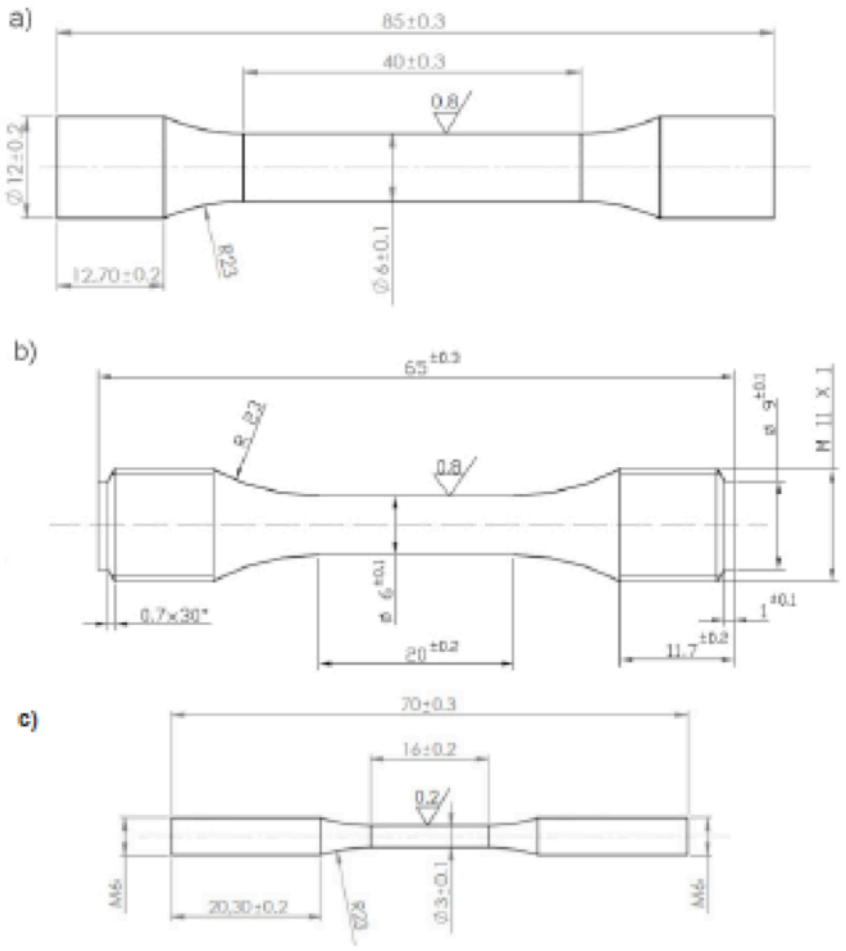

Figure 4: specimen geometry: a) static, b) HCF, c) LCF characterization

The procedure to calibrate the CIEL model parameters through the experimental data follows two steps, the first one is devoted at explaining how the parameters corresponding to the mean stress-strain coefficient f_{ms} can be estimated, while the second one deals with the calibration of the high temperature coefficient f_{ht}.

3.1. Calibration of the mean stress-strain coefficient f_{ms}

To estimate the values of the four parameters (η, h, ξ, and k) related to coefficient f_{ms}, isothermal LCF tests with mean stress and mean strain different from zero were performed (experimental detailed description in [45]), according to working conditions that will be considered in the FE simulation.

The evaluation of the mean stress effect on the material response can be performed both by means of stress-controlled and strain-controlled tests.

In the first case, usually the plastic deformation causes cyclic ratcheting strain, so the plastic strain

accumulation induces an additional damage, which results in a shorter life. In the second case, the plastic strain causes a mean stress relaxation in early life, therefore the fatigue life will not be appreciably affected. Usually mean strain effects become non negligible only if fatigue life is shorter than 10^3 cycles, for most engineering materials [25, 60].

Both the test conditions were adopted in the research work; Table 5 summarizes the experimental tests developed for the calibration of the parameters involved in the definition of coefficient f_{ms}. The reported amplitude ratios A are defined as σ_a/σ_m and $\varepsilon_a/\varepsilon_m$, where stress and strain are the total mechanical corresponding values (elastic and plastic contributions). The total strain values were selected to accurately describe the cyclic plastic behaviour of the material.

Table 5: Experimental tests to calibrate f_{ms}.

LCF test	**T [°C]**	**σa [MPa]**	**σm [MPa]**	***A***
Stress-controlled	160	400	50	8
		400	100	4
		400	200	2
LCF test	**T [°C]**	**εa [MPa]**	**εm [MPa]**	***A***
Strain-controlled	160	0,3%	0,05%	6
		0,3%	0,10%	3
		0,3%	0,15%	2

According to Eq. (5), in presence of mean stress and/or mean strain the equivalent stress amplitude $\sigma_{a,eq\text{-}1}$ and the equivalent strain amplitude $\varepsilon_{a,eq\text{-}1}$, which give the same fatigue life in the fully-reversed loading condition, can be determined. To do this, another set of experimental work was performed in fully-reversed loading conditions (R = -1) [45, 64] to obtain the BMC parameters involved in the complete BMC strain-life equation,

$$\varepsilon_a = \frac{\sigma_f'}{E}\left(N_f\right)^b + \varepsilon_f'\left(N_f\right)^c \tag{10}$$

The corresponding values of σ_f', b, ε_f' and c are reported in Table 6; these results are consistent with [44].

Table 6, Estimated values of the Basquin-Manson-Coffin parameters.

T [°C]	**σ_f' [MPa]**	***b***	**ε_f'**	***c***
160	2857	-0,2205	0,1221	-0,7199

500	1596	-0,2127	0,0721	-0,4619
800	585	-0,1892	0,0349	-0,5878

These equivalent stress and strain were then respectively introduced into the Basquin and the Manson-Coffin laws, to establish the relationship between stress, strain and fatigue life,

$$\sigma_{a,eq-1} = \frac{\sigma'_f}{E}\left(2N_f\right)^b \quad \text{and} \quad \varepsilon_{a,eq-1} = \varepsilon'_f\left(2N_f\right)^c \tag{11}$$

Then the set of stress-controlled and strain-controlled tests at three different amplitude ratios A (Table 5) were performed acquiring the corresponding number of cycles to failure N_f which can be introduced into Eq. (11) to determine the value of $\sigma_{a,eq-1}$ and $\varepsilon_{a,eq-1}$ equivalent to the fully-reversed loading condition (R = -1). Rewriting Eq. (5),

$$\frac{\sigma_{a,eq-1}}{\sigma_a} = \left(1+\eta\frac{\sigma_m}{\sigma_a}\right)^h \quad \text{and} \quad \frac{\varepsilon_{a,eq-1}}{\varepsilon_a} = \left(1+\xi\frac{\varepsilon_m}{\varepsilon_a}\right)^k \tag{12}$$

where η and h, ξ and k, can be determined respectively by fitting the experimental data on a plot $\sigma_{a,eq-1}/\sigma_a$ - σ_m/σ_a and a plot $\varepsilon_{a,eq-1}/\varepsilon_a$ - $\varepsilon_m/\varepsilon_a$.

In Table 7 the resulting values of the four parameters η and h, ξ and k of the mean stress-strain coefficient f_{ms} are summarized.

Table 7, Estimated values for η and η, ξ and κ

η	h	ξ	k
3,789	1,104	2,523	1,520

3.2. Calibration of the high temperature coefficient f_{ht}

The definition of the high temperature coefficient f_{ht} requires to know the values of the activation temperature T_{act} for creep and of the melting temperature T_{melt}. In the present research the first one was set equal to 530 °C, i.e. 1/3 of the melting temperature of 1600 °C. In addition, the parameter n of the Norton's law was found in literature [65] for the Si-Mo-Cr cast iron, and it is assumed n = 4. Therefore, the exponent b can be evaluated performing LCF tests at different temperatures. In the case of the commercial exhaust manifold investigated, the considered temperature range is 160 °C - 800 °C, hence 160 °C was assumed the threshold level below which no temperature effects on

fatigue occur. The value of K_s was determined at this temperature level, so no corrections are needed at 160 °C.

A dedicated Matlab ® routine was implemented to calculate K_s and U_i for each investigated temperature level as the sum of the areas of the hysteresis loops of all the cycles until failure. For each temperature level, K_s was estimated using the experimental data at 0,3% of total strain amplitude. In Table 8 the measured values of K_s and U_i for each temperature level are summarized.

Table 8, Values of K_s and U_i at different temperatures

T [°C]	K_s [J/mm^3]	U_i [J/mm^3]		
		$\varepsilon_{a,tot}$ 0,3%	$\varepsilon_{a,tot}$ 0,4%	$\varepsilon_{a,tot}$ 0,5%
160	0,644	$4{,}521 \cdot 10^{-4}$	$9{,}625 \cdot 10^{-4}$	$2{,}016 \cdot 10^{-3}$
500	1,785	$5{,}459 \cdot 10^{-4}$	$1{,}386 \cdot 10^{-3}$	$2{,}329 \cdot 10^{-3}$
800	0,057	$5{,}993 \cdot 10^{-4}$	$1{,}357 \cdot 10^{-3}$	$1{,}722 \cdot 10^{-3}$

The experimental tests confirmed that the Si-Mo-Cr ductile cast iron of the commercial exhaust manifold is characterized by higher fatigue resistance at 500 °C than at 160 °C; on the contrary, moving to 800 °C the fatigue strength drops. The estimation of exponent b was then carried out by means of the experimental data at 500 °C and 800 °C, by means of varying the value of b and minimizing the mismatch between the experimental life of the specimens and the predictions achieved. When $b = 14$, the difference between simulated and actual life of specimens reaches the minimum value that is below 9%.

4. Results and discussion

The capabilities of the energy-based life model were investigated first applying it to the uniaxial case represented by the specimens and comparing the experimental endurances acquired by the material characterization tests with the corresponding life predictions. The second investigation consisted in estimating the life of the exhaust manifold and comparing the prediction with a reference experimental endurance. This reference endurance was assumed equal to 3400 cycles, which value was found in literature for a very similar component subjected to almost the same both the specimens and the exhaust manifold cases, the comparison with the life predictions computed applying several literature damage models was also analysed.

For all the calculations, the value of K_s corresponding to 160 °C only was used because this temperature was considered as the reference one.

4.1. Specimens life predictions

As specimen testing was performed at R = -1, in Eq. (6) only the influence of temperature was taken into account. Two different sets of specimens were used for model calibration and validation. Table 9 and Table 10 report the experimental cycle to failure results for each temperature and total strain amplitude value tested. Each N_{exp} value is the average value obtained on at least three specimens. Percent standard deviation of experimental data is lower than 17%. In Table 9 life estimations of CIEL model are obtained by means of calibrating the model at 160 °C and 0,3% of strain amplitude; while S and BMC predictions are obtained by means of calibrating the models at the corresponding temperature. The % differences between the actual experimental life and the predicted ones are also indicated.

Table 9: Experimental cycles to failure, CIEL, S and BMC model cycles to failure estimations of specimens and % differences between life estimation and experimental life

T [°C]	εa	*Nexp*	CIEL		S		BMC	
			N	*diff%*	*N*	*diff%*	*N*	*diff%*
160	0,3%	1423,7±13,4%	1424	0,0	1424	0,0	1800	+26,4
	0,4%	715,0±9,0%	669	-6,4	669	-6,4	712	-0,4
	0,5%	392,3±16,4%	319	-18,6	319	-18,6	361	-7,9
500	0,3%	3273,7±7,1%	3090	-5,6	3270	-0,1	3232	-1,3
	0,4%	1292,0±7,0%	1223	-5,3	1288	-0,3	1352	+4,6
	0,5%	789,3±5,3%	740	-6,2	766	-2,9	717	-9,1
800	0,3%	95,7±11,0%	98	+2,1	95	-0,9	143	+49,0
	0,4%	46,3±10,9%	42	-8,7	42	-8,7	66	+43,5
	0,5%	31,7±10,2%	34	+6,3	33	+3,4	39	+21,9

Figure 5 compares the life predictions achieved by BMC, S and CIEL models with the experimental life of the specimens measured at each temperature level.

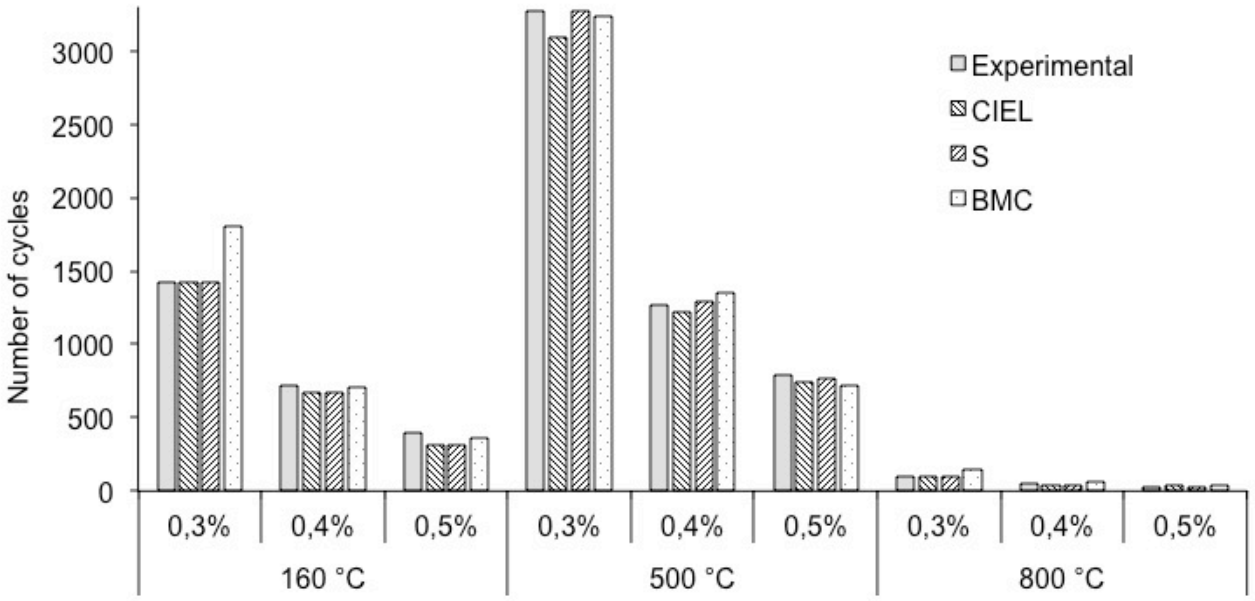

Figure 5: S, BMC, CIEL model life predictions and experimental life of specimens at each temperature level.

In Table 10 a focus on S model is reported. In particular, three sets of life predictions are reported by means of calibrating the model at 160 °C, 500 °C, and 800 °C respectively. The % differences between the actual experimental life and the predicted ones are also indicated.

Table 10: Experimental cycles to failure and S model cycles to failure estimations of specimens and % differences between life estimation and experimental life, with different calibration setting.

T [°C]	ε_a	*Nexp*	S					
			160 [°C]		500 [°C]		800 [°C]	
			N	*diff%*	*N*	*diff%*	*N*	*diff%*
160	0,3%	1423,7±13,4%	1424	0,0	3948	+177,3	126	-91,1
	0,4%	715,0±9,0%	669	-6,4	1855	+159,4	59	-91,7
	0,5%	392,3±16,4%	319	-18,6	885	+125,9	28	-92,8
500	0,3%	3273,7±7,1%	1180	-64,0	3270	-0,1	104	-96,8
	0,4%	1292,0±7,0%	465	-64,0	1288	-0,3	41	-96,8
	0,5%	789,3±5,3%	277	-65,0	766	-2,9	24	-96,9
800	0,3%	95,7±11,0%	1075	+1019,4	2978	+3002,6	95	-0,9
	0,4%	46,3±10,9%	475	+931,7	1315	+2759,6	42	-8,7
	0,5%	31,7±10,2%	374	+1068,7	1037	+3139,3	33	+3,4

Referring to Table 9, at 160 °C, at 0,3% and 0,4% of total strain amplitude the mismatch between the life predictions achieved by the CIEL and the experimental life of the specimens is within 7%, while at 0,5% of total strain amplitude the mismatch grows to 19% thus exceeding the experimental life scatter. This higher mismatch is due to the scattering of the experimental data at this

temperature level that makes the mean experimental life considered less meaningful than in the other temperature conditions, as discussed in [45]. It is possible to note that CIEL and S models give the same life predictions; this is justified by the fact that 160 ˚C was considered as the reference temperature for the proposed CIEL model. It has to be also noted that for the strain amplitude of 0,3%, the BMC model even exceeds the experimental life scatter.

At 500 ˚C, the CIEL model underestimates the life for all the total strain amplitudes applied, with an average mismatch of -5,7%. In the same situation, the S model estimations are within -2,9% while the BMC model estimations vary within -9,1% and +4,6%. BMC model shows an evident sensitivity with respect to loading and temperature variation. Apparently, at this temperature, the CIEL model predictions are worst if compared with the S ones obtained with the 500 ˚C S model calibration; but if these results are compared with the S life predictions obtained with the 160 °C S model calibration (Table 10) the CIEL model results to be more reliable.

The same behaviour can be observed at 800 ˚C, CIEL model life estimations obtained with 160 ˚C calibration are comparable with those of S model calibrated at 800 °C, but are more reliable than those of S model calibrated at 160 ˚C. In detail, at 800 ˚C CIEL model overestimates the experimental life at 0,3% and 0,5% of total strain amplitude, while at 0,4% it underestimates the life showing a mismatch of about 9%. Finally, at 800 ˚C the advantage provided by the Skelton and the CIEL model is evident, the maximum mismatch is lower than 9% while the BMC model overestimates the life more than 20% and up to almost 50%, a not acceptable result which confirms the limitations of the BMC model in very high temperature applications.

CIEL model calibration performed in other combinations of stress, strain and temperature was applied to obtain life estimation in different conditions. The CIEL model prediction ability was confirmed.

In the present paper the results related to calibration of CIEL model at lower temperature was reported as it is the easiest and cheaper to be performed in a laboratory.

4.2. Exhaust manifold life predictions

For the FE thermo-structural analysis, a whole exhaust system was modelled (exhaust manifold, gasket, cylinder head simulacrum, bolts) with the aim of determining the exhaust manifold temperature maps and stress-strain field. The geometry was obtained by means of cutting in slices and measuring the obtained cross sections of a commercial exhaust manifold from a 1.9l 4-cylinders compression ignition IC engine.

Simulation software was ABAQUS 6.9-3; 4-node TETRA4 and 10-node TETRA10 tetrahedral elements were used for the solid mesh. The mesh of all surfaces has been defined using the automatic tools of the code, optimizing the elements geometry only in few narrow areas, for instance the zone in which manifold runners converge; elements with an excessive distorsion have been deleted and manually rebuilt. On the cylindrical surfaces of the through bolt holes a mesh control has been imposed to obtain the best nodes alignment: a condition of cylindricity has been imposed, with 16 nodes placed on the hole's edge. The solid mesh of the model has been built with TETRA4 elements for the thermal analysis and TETRA10 elements for the structural analysis. Once the mesh has been completed, the elements order has been changed through a dedicated tool without changing the nodes disposition.

The two-dimensional mesh has been used as a guide for the realization of the solid mesh.

In this phase a very efficient mesh tool implemented in SimLab 8.0 has been used: this tool allows to select all the two-dimensional meshes which have to be used as reference for the solid mesh, with the possibility to choose the number of elements to be placed in the thickness of the model. In this way in the smallest thicknesses of the manifold has been placed at least two elements in order to increase the quality of the results.

The adoption of first-order or second-order solid elements was imposed by the typology of the performed analysis. In thermal analysis, first-order elements with thermal degree of freedom for calculation of temperature distributions, while second-order elements were used for structural analysis to avoid stiffness overestimation. The gasket and the cylinder head simulacrum are introduced in the complete FE model as constraints and boundary conditions. The mean dimensions of the adopted finite elements for the manifold mesh are considerably smaller compared with those of the cylinder head simulacrum; the gasket elements are comparable in terms of dimensions with those of the manifold itself. The total number of nodes of the manifold is 61005, while 122086 are the TRIA3 elements. For the gasket, the total number of nodes is 9372, while 18788 are the TRIA3 elements. For the cylinder head simulacrum, the total number of nodes is 11460, while 22936 are the TRIA3 elements.

The parameters imposed for the definition of the manifold solid mesh elements are therefore summarized in the following Table 11.

Table 11: Parameters adopted in the solid mesh of the model

Parameter value	
Average element size	2 mm
Aspect ratio	20
Stretch	<0.1
Skew	<90

Collapse ratio	<0.05
Skewness	<0.02
Interior angle	10÷160
Tet collapse	<0.12
Distorsion	<0.01
Jacobian	<0.1

The thermal analysis took into account of all the heat exchange conditions referring to the gas and the solid parts of the model and all the interactions between them. The considered heat exchange phenomena are: convection between the gas and the solid parts of the model, convection between the model and the environment, and conduction between each contacting part. To obtain the thermal exchange parameters required for the exhaust manifold thermal analysis, a Computational Fluid Dynamic (CFD) analysis, consisting of a coupled fluid-structure CFD steady-state simulation at maximum engine spin speed, was previously done. The resulting thermal contour worked as thermal loading condition for the subsequent structural analysis of the exhaust manifold.
For what concerns the constitutive material models, the exhaust manifold cast iron behaviour was modelled using a temperature dependent elasto-plastic constitutive model in which cyclic plasticity is estimated by a non-linear isotropic-kinematic hardening network. Material data are input from experimental static and cyclic testing. In particular the calibration of the ABAQUS non-linear isotropic-kinematic hardening model is based on two steps [66]. The first one is the definition of the isotropic hardening component of the model, represented by the evolution of the equivalent stress defining the size of the yield surface, as a function of the equivalent plastic strain. To do this, a list of tabular data obtained from the cyclic tests has been specified. More in details, from the LCF experimental data the peak stress values in tension and the correspondent yield stresses in compression for each cycle have been processed. In order to calibrate also the kinematic component of the model, the stress-strain data defining the stabilized cycles of the different tests were processed. The constitutive model was calibrated for each temperature level and at the maximum strain range applied, maintaining then the same calibration for all the other isothermal strain ranges. For the cylinder head simulacrum aluminium alloy and for the steels of the gasket and the bolts, linear elastic constitutive models was used, without taking into account the temperature dependence of parameters. In addition to the thermal loads caused by the engine functioning, the exhaust manifold is also subjected to several time-independent mechanical loads, mainly represented by the turbocharger system weight and the bolts load. The weight of the turbocharger system was introduced under the hypothesis that no support brackets are present, so all the turbocharger system weight of 4 kg was applied to the corresponding collar of the exhaust manifold. The structural transient analysis of the exhaust manifold was performed setting several Static general calculation

steps in ABAQUS CAE. Four thermal cycles were simulated, between 160 and 180 °C. The thermal model allows to compute the transient temperature distribution of the exhaust manifold due to the application of the four exhaust gas thermal cycles defined. The aim of the following structural analysis is therefore to estimate the displacement, the stress, and the strain field resulting from the temperature variations. In the last computation step, the four thermal cycles defined in the thermal analysis have been applied by importing the nodal temperature evolution of the model. Consequently, the simulation time for this step is equal to 3040 s, while the maximum calculation time interval has been set to 1 s. Results have been required for 60 equally spaced time instants during the simulation in order to achieve a good compromise between a sufficiently detailed stress-strain history and the size of the results file.

By using five literature multi-axial damage criteria (von Mises (vM) [67], ASME code [68], Sonsino-Grubisic (SG) [41], Kandil-Brown-Miller (KBM) [42], and Fatemi-Socie (FS) [43]) and the results obtained from the FE thermo-structural transient analysis, the corresponding values of the equivalent strain amplitude were computed. Introducing these equivalent strain amplitudes into the BMC model, previously calibrated with the experimental data (see Table 6), the corresponding life estimations of the exhaust manifold were computed. The component residual life was also estimated by using the CIEL and S models.

All the life predictions were performed for each of the four critical zones of the manifold detected through the FE analysis, identified in Figure 6 as points 1, 2, 3 and 4. The corresponding stress and strain results are showed in Figure 7 to 10.

The stress along two main directions of the manifold were also investigated, with the aim to better understand the nature of the stress field. In this way in fact it is possible to clarify if the manifold is subjected to tensile or compressive stress and, consequently, if the critical areas previously detected may be potential nucleation sites for fatigue cracks. The two directions along which stresses are investigated are defined by the fictitious line linking the centers of the ducts on the main flange plane and by the axes of the bolts holes; these directions are called x and y, respectively. The results are presented in Table 10. The hysteresis loops were then plotted for the investigated elements to obtain the dissipated energy per cycle. An example is reported in Figure 11 .

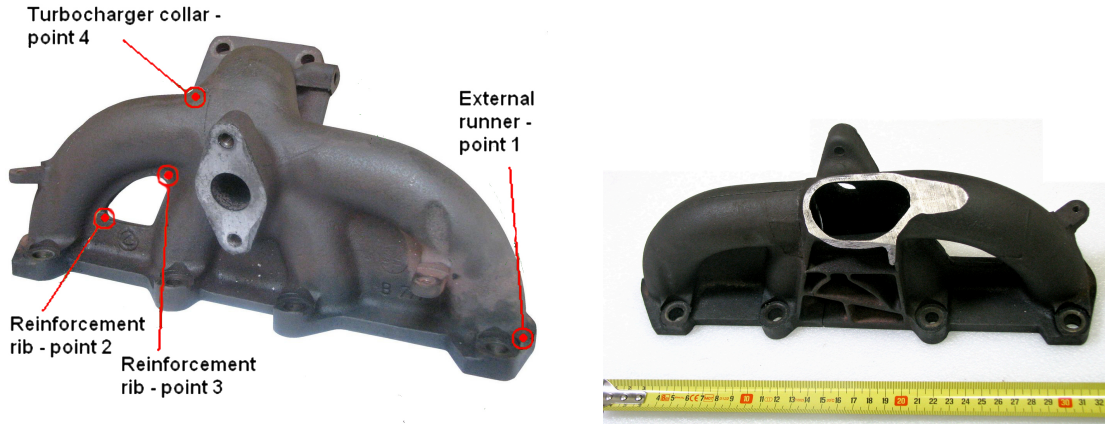

Figure 6: Exhaust manifold critical points (EGR side).

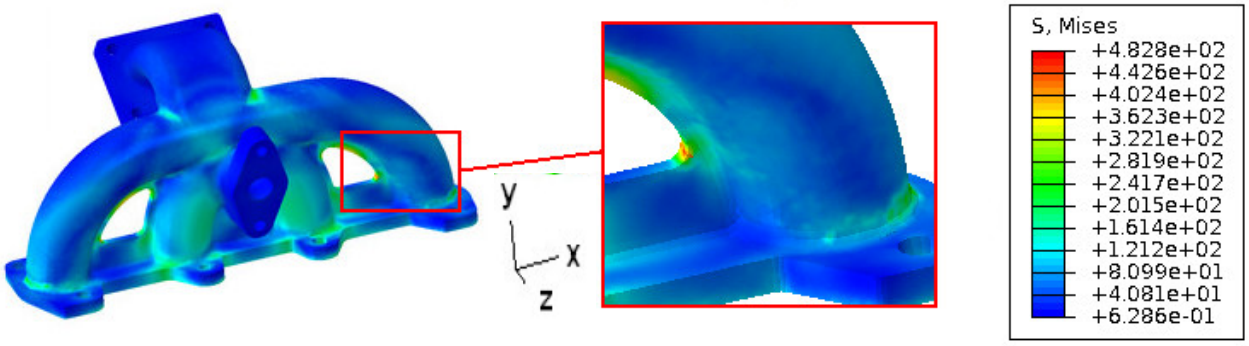

Figure 7: Example of FE analysis result. Von Mises stress in MPa

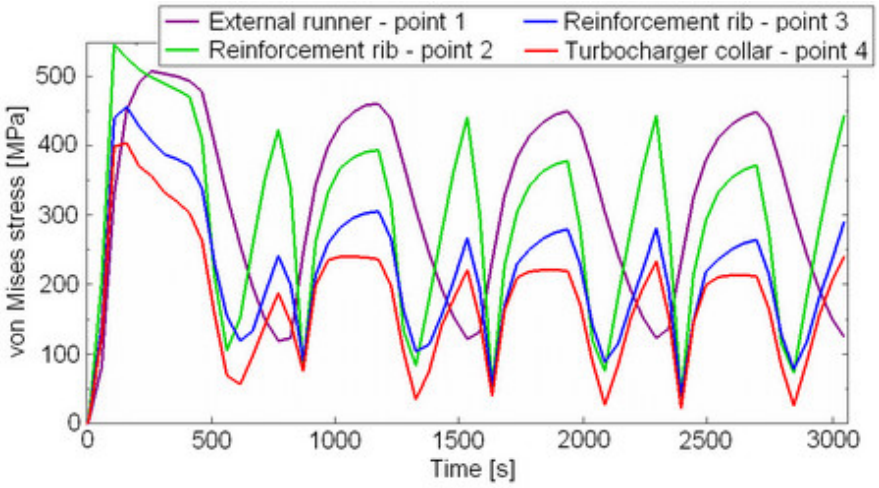

Figure 8: Time evolution of the von Mises stress for the elements investigated.

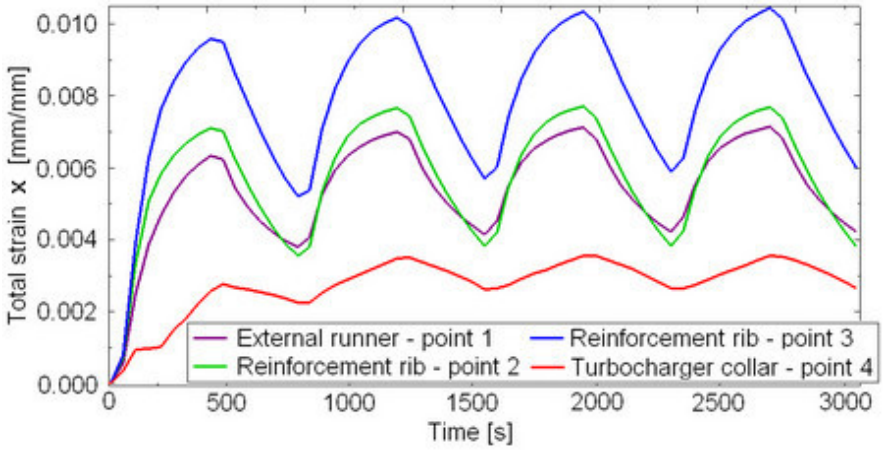

Figure 9: Time evolution of the total strain along x direction for the elements investigated.

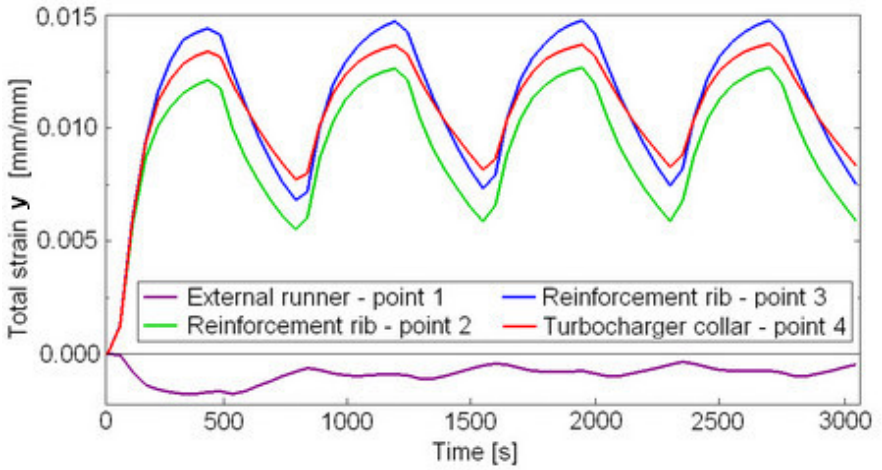

Figure 10: Time evolution of the total strain along *y* direction for the elements investigated

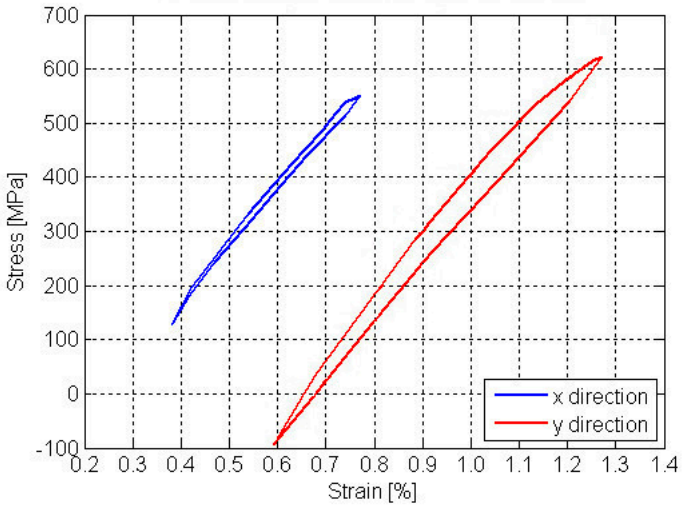

Figure 11: Stabilized hysteresis loops of the element 2

A representative temperature of the last thermal cycle imposed in the simulation, which is

considered the stabilised one, was computed as the arithmetic mean of the temperature values defining the cycle itself. It has to be noted that in most of the analytical formulations of literature damage models the temperature does not appear as an explicit variable. The BMC model, on which many multi-axial criteria are based, has to be in fact calibrated using isothermal LCF data, in analogy with the S model, where the constant K_s has to be estimated for each temperature. It follows that, when the application under investigation is characterised by wide thermal cycles applied, as in the case of the exhaust manifold analysed in this research work, several problems may arise. However, this critical point can be bypassed estimating an equivalent temperature for the thermal cycles, that is a temperature level giving, if applied in isothermal low cycle fatigue conditions, the same fatigue life than non-isothermal fatigue. For this purpose, the early works proposed in [60] and the following recent developments of [69, 70] are particularly interesting.

The parameters of BMC model and those of S and CIEL models, corresponding to this mean temperature of each investigated point, were calculated interpolating linearly the known values at the three temperature levels of the experimental tests. Furthermore, the S model and the CIEL model were applied considering the stabilized hysteresis loop along both x and y direction investigated to understand which components of the stress and strain tensor is the most damaging. For each critical point analysed the variables required by the energy-based models, (mean stress, mean strain and maximum tensile stress) were then extrapolated from the corresponding stabilized hysteresis loops. It has to be noted that, according to Skelton model, for a given total strain range, the hysteresis energy per cycle, U_i, is almost independent of the stage of hardening or softening. Such attributes have been considered valid to make the energy criterion a worthy candidate for describing crack tip conditions. The model assumes that the process zone depth is constant for all conditions, the peak energy density therein for a single loading cycle is uniform and that the zone fails when the accumulated energy density after N applied cycles reaches a critical value, Ks. The crack then moves forward by an amount whereupon energy begins to build up in a new process zone.

All damage models (both multi-axial and energy-based) highlight that the most critical zone for the structural integrity of the exhaust manifold corresponds to the reinforcement rib between the external runner and the manifold flange (point 2 of Fig. 4). Referring to the most critical zone (point 2 of Figure 6) of the exhaust manifold, Table 12 reports the total energy expenditure until fracture and the energy dissipated by the exhaust manifold FE model, computed by using CIEL and S models.

Table 12: Total energy expenditure until fracture and energy dissipated by the exhaust manifold FE model.

Model	Ks [J/mm^3]	Direction	U_i [J/mm3]
CIEL	0,644	x	0,1430±10^{-3}
		y	0,3089±10^{-3}
S	1,144	x	0,1430±10^{-3}
		y	0,3089±10^{-3}

A reference experimental endurance of 3400 cycles was found in literature for a very similar exhaust manifold subjected to almost the same loading and temperature conditions (250-650 °C vs 160-800°C of the present paper) [71, 72, 73] and a very similar composition. In Table 13 the equivalent strain amplitudes, computed with several multi-axial damage criteria, are summarized together with the life predictions computed by CIEL, S, and BMC model for all the reported multi-axial criteria. The % differences between the literature experimental life and the predicted ones are also indicated. CIEL and S models are used with the total energy expenditures until fracture and the energies dissipated (maximum values) of Table 12.

Table 13: Equivalent strain amplitude computed with different multi-axial damage criteria, and corresponding cycles to failure estimations of the exhaust manifold.

Model	$\varepsilon a,eq$	N	diff%
CIEL	-	3262	-4.1
S	-	3703	+8.9
vM [67]	0,26%	4065	+19.6
ASME [68]	0,25%	4271	+25.6
SG [41]	0,23%	4843	+42.4
KBM [42]	0,33%	3648	+7.3
FS [43]	0,25%	5730	+68.5

Figure 12 shows the comparison between the life predictions obtained by all the damage models applied to the exhaust manifold, in terms of number of cycles predicted for the most critical zone, and the reference endurance of 3400 cycles. For S and CIEL models the shortest life between the two x and y investigated directions is reported (3703 and 3262 cycles respectively).

The CIEL model results to be the most conservative one, underestimating with a closer value the exhaust manifold actual life. This result, if considered applied to commercial components involving human use, is in favour of safety.

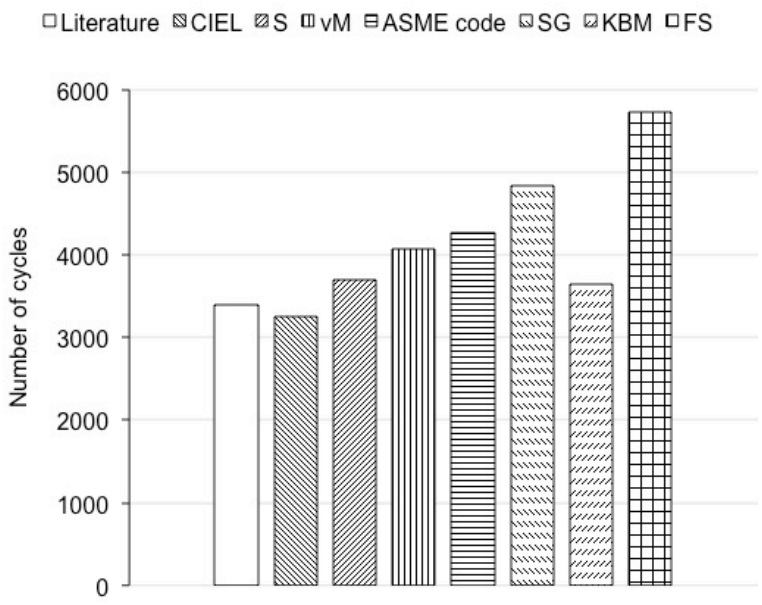

Figure 12: Comparison between the life predictions obtained for the exhaust manifold.

5. Conclusions

A new energy-based life model is proposed. It was developed on the basis of Skelton model also taking into account of mean stress and high variable temperature effects on fatigue.

The fundamental idea was the correction of the total expended energy to failure K_s, estimated under isothermal and no mean stress conditions. In particular, two empirical coefficients were introduced, which task is to modify the value of K_s if mean stress or high temperature effects occur, according to experimental observations.

The comparison between experimental and predicted life of specimens has pointed out the prediction capabilities of the new energy-based life model in all the testing conditions, including different strain amplitudes and different temperature values. The results were compared with Skelton and Basquin-Manson-Coffin predictions. Skelton and BMC models were calibrated in each testing conditions, while CIEL was calibrated only in one condition. Despite this calibration disadvantage, CIEL model always showed predicted percentage differences lower than 9% (except in one case) with respect to experimental results. Skelton model showed comparable predictions, but only if calibrated in each testing condition. Basquin-Manson-Coffin model predictions are comparable, but only for temperatures lower than 500 °C and needing dedicated calibration. CIEL model results to maintain the same reliability also in testing condition far from calibration ones. The advantage of the CIEL model lies then in a wider range of applicability.

The application of CIEL model was then extended to the case study of a commercial exhaust

manifold. The CIEL model provided results close to the Kandil-Brown-Miller model, which was proved to be one of the most suitable multi-axial literature damage models to be used in high temperature LCF and TMF. Furthermore, the detection of the most critical area for fatigue failure in the component is coherent with the literature models, and the life predicted for the critical element is very close to the reference endurance found in literature.

A further advantage of CIEL model is that it is constituted by five parameters only, four related to mean stress effects and one related to high temperature influences. Consequently, a reduced experimental calibration effort is required, consisting in six LCF tests under different mean stress and strain conditions and three LCF tests under different isothermal conditions.

References

1. Danzer R. *Lebensdauerprognose hochfester metallischer Werkstoffe im Bereich hoher Temperaturen*. Berlin-Stuttgart: Gebruder Borntraeger, 1988.
2. Neu RW, Sehitoglu H. Thermomechanical fatigue, oxidation, and creep, Part I. damage mechanisms. *Metallurgical Transactions A*; 1989, 20A: 1755-67.
3. Neu RW, Sehitoglu H. Thermomechanical fatigue, oxidation, and creep, Part II. life prediction. *Metallurgical Transactions A*; 1989, 20A: 1769-83.
4. Minichmayr R, Riedler M, Winter G, Leitner H, Eichlseder W. Thermo-mechanical fatigue life assessment of aluminium components us ing the damage rate model of Sehitoglu. *International Journal of Fatigue*; 2008, 30(2): 298-304.
5. Coffin LF. A study of cyclic-thermal stresses in a ductile metal. *Trans ASME*; 1954; 76: 931-50.
6. R. HG, Manson SS. Life prediction of thermal-mechanical fatigue using strain range partitioning. West Conshohocken, PA, USA. In: *Thermal fatigue of materials and components*. ASTM STP 612: ASTM International 1976, 239-254.
7. Zamrik SY, Renauld ML. Thermo-mechanical out-of-phase fatigue life of overlay coated IN-738LC gas turbine materials. West Conshohocken, PA, USA. In: *Thermomechanical fatigue behaviour of materials, third volume*. ASTM STP 1371: ASTM International 2000, 119-137.
8. Halford GR, Lerch BA, Arya VK. Thermal strain fatigue modelling of a matrix alloy for a metal matrix composite. West Conshohocken, PA, USA. In: *Thermomechanical fatigue behaviour of materials, third volume*. ASTM STP 1371: ASTM International 2000, 186-203.
9. Chaboche JL. Continuum damage mechanics, present state and future trends. *Nuclear*

Engineering and Design; 1987, 105: 19-33.

10. Chaboche JL, Lesne PM. A non-linear continuous fatigue damage model. *Fatigue and Fracture of Engineering Materials and Structures*; 1988, 11: 1-17.
11. Lemaitre J, Chaboche JL. *Mechanics of Solid Materials*. New York, NY, USA; Cambridge University Press, 2000.
12. Skelton RP. *Crack initiation and growth in simple metal components during thermal cycling*. London, UK: Applied Science Publishers, 1983.
13. Jordan EH, Meyers GJ. Fracture mechanics applied to nonisothermal fatigue crack growth. *Engineering Fracture Mechanics*; 1986, 23 (2): 345-58.
14. Miller MP, McDowell DL, Oehmke RLT, Antolovich SD. A life prediction model for thermomechanical fatigue based on microcrack propagation. West Conshohocken, PA, USA. In: *Thermomechanical fatigue behaviour of materials*. ASTM STP 1186: ASTM International 2003, 35-49.
15. Dai J, Marchand NJ, Hongoh M. Thermal mechanical fatigue crack growth in titanium alloys, experiments and modelling. West Conshohocken, PA, USA. In: *Thermomechanical fatigue behaviour of materials, second volume*. ASTM STP 1263: ASTM International 1996, 187-209.
16. Kadioglu Y, Sehitoglu H. Thermomechnical and isothermal fatigue behaviour of bar and coated superalloys. *Journal of Engineering Materials and Technology (Trans ASME)*; 1996, 118: 94-102.
17. Christ HJ, Jung A, Maier HJ, Teteruk R. Thermomechanical fatigue. Damage mechanisms and mechanism-based life prediction methods. *Sadhana - Academy Proceedings in Engineering Sciences*; 2003, 28A: 147-65.
18. Seifert T, Riedel H. Mechanism-based thermomechanical fatigue life prediction of cast iron. part I, Models. *International Journal of Fatigue*; 2010, 32: 1358-67.
19. Seifert T, Maier G, Uihlein A, Lang KH, Riedel H. Mechanism-based thermomechanical fatigue life prediction of cast iron. part II, Comparison of model predictions with experiments. *International Journal of Fatigue*; 2010, 32; 1368-77.
20. Feltner CE, Morrow J. Microplastic strain hysteresis energy as a criterion for fatigue fracture. *Journal of Basic Engineering, ASME Transactions*; 1961, 83D: 15-22.
21. Morrow J. Cyclic plastic strain energy and fatigue of metals. West Conshohocken, PA, USA. In: *Internal friction, damping and cyclic plasticity*. ASTM STP 378: ASTM International 1965, 45-87.
22. Garud YS. A new approach to the evaluation of fatigue under multiaxial loadings. *Journal*

of Engineering Materials and Technology; 1981, 103: 118-26.

23. Filippini M, Foletti F, Papadopoulos IV, Sonsino CM. A multiaxial fatigue life criterion for non-symmetrical and non-proportional elasto-plastic deformation. New York, NY, USA, In: *Biaxial/Multiaxial Fatigue and Fracture* Volume 31. Elsevier ESIS Publication 2003, 383-400.
24. Ellyin F, Golos K. Multiaxial fatigue damage criterion. *Journal of Engineering Materials and Technology*; 1988, 110: 63-8.
25. Ellyin F, Kujawski D. A multiaxial fatigue criterion including mean stress effect. West Conshohocken, PA, USA, In: *Advances in Multiaxial Fatigue*. ASTM STP 1191: ASTM International 1993, 55-66.
26. Ellyin F. Effect of tensile-mean-strain on plastic strain energy and cyclic response. *Journal of Engineering Materials and Technology, Trans. ASME*; 1985, 107: 119-125.
27. Esin A. Prediction of the cyclic hardening stress-strain curve. Journal of Strain Analysis; 1980, 15: 235–237.
28. Skelton RP. Energy criterion for high temperature low cycle fatigue failure. *Material Science and Technology*; 1991, 7: 427-39.
29. Skelton RP, Vilhelmsen T, Webster GA. Energy criteria and cumulative damage during fatigue crack growth. *International Journal of Fatigue*; 1998, 20 (9): 641-9.
30. Schutz W. Uber eine beziehung zwischen der lebensdauer bei konstanter und veranderlichen beanspruchungsamplituden und ihre anwendbarkeit auf die bemessung von ugzeugbauteilen. *Zeitschrift fur Flugwissenschaften*;1967, 15: 407-19.
31. Gocmez T, Awarke A, Pischinger S. A new low cycle fatigue criterion for isothermal and out-of-phase thermomechanical loading. *International Journal of Fatigue*; 2010, 32 (4): 769-79.
32. Tanaka K, Mura T. A Dislocation Model for Fatigue Crack Initiation. *Journal of Applied Mechanics*; 1981, 48: 97-103, https://doi.org/10.1115/1.3157599.
33. Brückner-Foit A, Xinyue H. Numerical Simulation of Micro-Crack Initiation of Martensitic Steel under Fatigue Loading. *International Journal of Fatigue*; 2006, 28 (9): 963-71. https://doi.org/10.1016/j.ijfatigue.2005.08.011.
34. Kramberger J, Jezernik N, Glodež S. Extension of the Tanaka – Mura Model for Fatigue Crack Initiation in Thermally Cut Martensitic Steels. *Engineering Fracture Mechanics*; 2010, 77: 2040-50. https://doi.org/10.1016/j.engfracmech.2009.12.003.
35. Glodež S, Jezernik N, Kramberger J, Lassen T. Numerical Modelling of Fatigue Crack Initiation of Martensitic Steel. *Advances in Engineering Software*; 2010, 41 (5): 823-29.

https://doi.org/10.1016/j.advengsoft.2010.01.002.

36. Baldissera P, Delprete C. The Formal Analogy between Tanaka-Mura and Weibull Models for High-Cycle Fatigue. *Fatigue and Fracture of Engineering Materials and Structures*; 2012, 35 (2): 114-21. https://doi.org/10.1111/j.1460-2695.2011.01598.x.
37. Branco R, Prates PA, Kotousov A. New methodology of fatigue life evaluation for multiaxially loaded notched components based on two uniaxial strain-controlled tests. International Journal of Fatigue; 2018, 111: 308-320.
38. Lazzarin P. A review of the volume-based strain energy density approach applied to V-notches and welded structures. Theoretical and Applied Fracture Mechanics; 2009, 52: 183-194.
39. Wang RZ, Zhu XM, Zhang CC. A generalized strain energy density exhaustion model allowing for compressive hold effect. International Journal of Fatigue; 2017, 104: 61-71.
40. Fang D, Berkovitz A. Mean stress models for low-cycle fatigue of a nickel-based superalloy. *International Journal of Fatigue*; 1994, 16(6): 429-37.
41. Sonsino CM, Grubisic V. Fatigue behaviour of cyclically softening and hardening steels under multiaxial elastic-plastic deformation. Philadelphia, PA, USA, In: *Multiaxial fatigue*. ASTM STP 853: ASTM International 1985, 586-605.
42. Kandil FA, Brown MW, Miller KJ. *Biaxial low-cycle fatigue fracture of 316 stainless steel at elevated temperatures*. London, UK, Book 280: The Metal Society, 1982.
43. Fatemi A, Socie DF. A critical plane approach to multiaxial fatigue damage including out-of-phase loading. *Fatigue and Fracture of Engineering Materials and Structures*; 1988, 11: 149-65.
44. Pevec M, Oder G, Potrc I, Srami M. Elevated temperature low cycle fatigue of grey cast iron used for automotive brake discs. *Engineering Failure Analysis*; 2014, 42: 221-30.
45. Delprete C, Sesana R. Experimental characterization of a SiMoCr ductile cast iron. Materials and Design; 2014, 57: 528-37.
46. Delprete C, Rosso C. Residual life estimation under low-cycle and thermo-mechanical fatigue conditions, Proposal of a dedicated numerical code. In, ASME 2014 - 12th Biennial Conference on Engineering Systems Design and Analysis; vol. 1. ISBN 978-0-7918-4583-7; 2014, doi,10.1115/ESDA2014-20458.
47. Chu CC. Comparison of mean stress correction methods for fatigue life prediction. *SAE Technical Paper 2000-01-0778*, 2000.
48. Kujawski D, Ellyin F. A unified approach to mean stress effect on fatigue threshold

conditions. *International Journal of Fatigue* 1995; 17(2): 101-6.
49. Dowling NE, Calhoun CA, Arcari A. Mean stress effects in stress-life fatigue and the walker equation. *Fatigue and Fracture of Engineering Materials and Structures*; 2009, 32: 163-79.
50. Penny RK, Marriott DL. *Design for Creep* 2nd Edition. New York, NY, USA: Chapman and Hall, 1995.
51. Kennedy AJ. *Processes of Creep and Fatigue in Metals*. Edinburgh, UK: Oliver and Boyd, 1962.
52. Norton FH. *The Creep of Steel at High Temperature*. New York, NY, USA: McGraw Hill, 1929.
53. Ludwik P. *Elemente der Technologischen Mechanik*. Berlin, D: Springer, 1909.
54. Soderberg CR. The interpretation of creep tests for machine design. *Trans ASME*; 1936, 58: 733-43.
55. McVetty PG. Creep of metals at elevated temperatures - the hyperbolic sine relation between stress and creep rate. *Trans ASME*; 1943, 65: 761-769.
56. Garofalo F. *Fundamentals of Creep and Creep-Rupture in Metals*. NewYork, NY, USA: Macmillan, 1965.
57. Harper J, Dorn JE. Viscous creep of aluminum near its melting temperature. *Acta Metallurgica*; 1957, 5(11): 654-65.
58. ASTM E8/E8M-09 Standard Test Methods for Tension Testing of Metallic Materials.
59. Skoglund P, Sjogren T, Moverare J. Fatigue and strength of new grey iron alloys for brake discs. In: *LCF-7 - 7th International Conference on Low Cycle Fatigue*, 2013, 45-50.
60. Payten WM, Dean DW, Snowden KU. A strain energy density method for the prediction of creep–fatigue damage in high temperature components. Materials Science and Engineering A; 2010, 527: 1920-1925.
61. Andrade E. *The viscous flow in metals and allied phenomena*. Proceedings of the Royal Society London; 1910, A(84): 1-12.
62. Bailey RW. *The Utilization of Creep Test Data in Engineering Design*. London, UK: Institution of Mechanical Engineers, 1935.
63. Taira S. Relationship between thermal fatigue and low-cycle fatigue at elevated temperatures. West Conshohocken, PA, USA, In: *Fatigue at elevated temperatures*. ASTM STP 520: ASTM International 1973, 80-101.
64. Vercelli A. *Design methodologies for high temperature low cycle fatigue of engine components*. Torino, I, PhD Thesis: Politecnico di Torino, 2011.
65. Webster GA, Ainsworth RA. *High Temperature Component Life Assessment*. London, UK:

Chapman and Hall, 1994.
66. ABAQUS Version 6.9 User's Manual. Dassault Systemés, 2009.
67. von Mises R. Mechanik der festen krper im plastisch deformablen zustand. *Göttin Nachr Math Phys*; 1913, 1: 582-92.
68. ASME. Class 1, components in elevated temperature service. New York, NY, USA, *Cases of ASME Boiler and Pressure Vessel Code, Section III, Division 1, Appendix T*; 1988.
69. Nagode M, Hack M. An online algorithm for temperature in fatigue life estimation, stress-life approach. *International Journal of Fatigue*; 2004, 26: 163-71.
70. Nagode M, Zingsheim F. An online algorithm for temperature in fatigue life estimation, strain-life approach. *International Journal of Fatigue*; 2004, 26: 155-61.
71. Constantinescu A, Charkaluk E, Lederer G, Verger L. A computational approach to thermomechanical fatigue. *International Journal of Fatigue*; 2004, 26: 805-18.
72. Lederer G, Charkaluk E, Verger L, Constantinescu A. Numerical life-time assessment of engine parts submitted to thermomechanical fatigue, application to exhaust manifold design. *SAE Technical Paper 2000-01-0789*; 2000.
73. Charkaluk E, Bignonnet A, Costantinescu A, Dan Van K. Fatigue design of structures under thermomechanical loadings. *Fatigue Fracture of Engineering Materials Structures*; 2002, 25: 1199-206.